CrossMark

ORIGINAL PAPER

The Influence of Temperature on Time-Dependent Deformation and Failure in Granite: A Mesoscale Modeling Approach

T. Xu[1,2] · G. L. Zhou[1,2] · Michael J. Heap[3] · W. C. Zhu[1,2] · C. F. Chen[1,2,3] ·
Patrick Baud[3]

Abstract An understanding of the influence of temperature on brittle creep in granite is important for the management and optimization of granitic nuclear waste repositories and geothermal resources. We propose here a two-dimensional, thermo-mechanical numerical model that describes the time-dependent brittle deformation (brittle creep) of low-porosity granite under different constant temperatures and confining pressures. The mesoscale model accounts for material heterogeneity through a stochastic local failure stress field, and local material degradation using an exponential material softening law. Importantly, the model introduces the concept of a mesoscopic renormalization to capture the co-operative interaction between microcracks in the transition from distributed to localized damage. The mesoscale physico-mechanical parameters for the model were first determined using a trial-and-error method (until the modeled output accurately captured mechanical data from constant strain rate experiments on low-porosity granite at three different confining pressures). The thermo-physical parameters required for the model, such as specific heat capacity, coefficient of linear thermal expansion, and thermal conductivity, were then determined from brittle creep experiments performed on the same low-porosity granite at temperatures of 23, 50, and 90 °C. The good agreement between the modeled output and the experimental data, using a unique set of thermo-physico-mechanical parameters, lends confidence to our numerical approach. Using these parameters, we then explore the influence of temperature, differential stress, confining pressure, and sample homogeneity on brittle creep in low-porosity granite. Our simulations show that increases in temperature and differential stress increase the creep strain rate and therefore reduce time-to-failure, while increases in confining pressure and sample homogeneity decrease creep strain rate and increase time-to-failure. We anticipate that the modeling presented herein will assist in the management and optimization of geotechnical engineering projects within granite.

Keywords Brittle creep · Temperature · Creep strain rate · Damage evolution · Numerical simulation

✉ T. Xu
xutao@mail.neu.edu.cn

1 Key Laboratory of Ministry of Education on Safe Mining of Deep Metal Mines, Northeastern University, Shenyang 110819, People's Republic of China

2 Center for Rock Instability and Seismicity Research, Northeastern University, Shenyang 110819, People's Republic of China

3 Laboratoire de Géophysique Expérimentale, Institut de Physique de Globe de Strasbourg (UMR 7516 CNRS, Université de Strasbourg/EOST), 5 rue René Descartes, 67084 Strasbourg Cedex, France

List of symbols

A	Material constant
D	Damage variable
E, E_0	Young's moduli of damaged material and undamaged material
F_{t0}, F_{c0}	Uniaxial tensile strength and uniaxial compressive strength
F_1, F_2	Tensile and shear damage threshold functions
G	Shear modulus
N	Total number of elements
R	Universal gas constant
S_{ij}	Stress deviator tensor of the elastic stress components
T, T_a	Temperature, ambient temperature

🙋 Springer

U	Creep activation energy
v_e	The volume of single element
V_f, V	The volume of failed elements, the total volume of all elements
c	Heat capacity of the medium
e_f	Energy released from a failed element
e_{ij}	Strain deviator of the elastic strain components
f_i	Body forces per unit volume
h	The convective heat transfer coefficient
k	Apparent thermal conductivity
m	A fraction constant
n	Stress component of greater than one
n_i	The number of failed elements in the ith step
q_i, q	The rate of heat conduction, heat source generated inside the medium
u, u_0	Scale parameter of an element, the average element parameter
u_i	Mechanical parameter of the element i
α	The coefficient of linear thermal expansion
β	The coefficient of thermal stress
δ_{ij}	Kronecker delta
λ	Lamé's constant
ρ	Bulk density of medium
χ	Homogeneity index
ϕ	Angle of internal friction
ω_i	Random numbers ranging from 0 to 1
ψ	The ratio of the volume of failed rock to total volume of rock
σ_e	Effective stress
σ_{ij}	Total stress tensor
σ_1, σ_2	The maximum and minimum principal stress
$\varepsilon_1, \varepsilon_3$	The maximum and minimum principal strain
$\varepsilon_{t0}, \varepsilon_{c0}$	The maximum tensile and compressive strain
ε	Total strain
ε_e	Elastic strain
ε_c	Creep strain
ε_T	Thermal strain
ε_{ij}	Elastic strain tensor

1 Introduction

Geological disposal is currently considered as the preferred option for waste management of long-lived radioactive waste worldwide. In a geological repository, which are designed to store and isolate waste over hundreds of thousands of years, the temperature in the near field will be increased due to the heat generated by the radioactive waste (Gibb 2000; Chu and Majumdar 2012). This sustained high temperature may have a significant influence on the time-dependent behavior of the host rock and consequently affect the overall long-term performance of the disposal. Therefore, a good understanding through the reliable modeling of the time-dependent behavior of the host rock at elevated temperatures is essential to the stability and safety analysis of nuclear waste disposal. Knowledge of the time dependence of rock deformation at elevated temperature is also important in geothermal reservoirs (e.g., Berard and Cornet 2003). Constraining the mechanical behavior of geothermal reservoir rock is important for resource management and optimization.

Extensive studies have been carried out on the time-dependent behavior of soft rocks like sedimentary rock and rock salt (Carter and Hansen 1983; Cristescu 1993; Dubey and Gairola 2008; Heap et al. 2009a, b; Brantut et al. 2014; Yang et al. 2014; Ye et al. 2015) and hard rocks like granite (Kranz 1980; Kranz et al. 1982; Lockner 1993a, b; Fujii et al. 1999; Katz and Reches 2002; Lin et al. 2009; Chen et al. 2015; Wang et al. 2015) and basalt (Heap et al. 2011). Granite is of particular importance in the context of nuclear waste disposal and geothermal energy. Granite is a widely recognized potential host rock for the disposal of nuclear waste due to its low permeability and high strength (Heuze 1983; Gibb 2000; Wang et al. 2006) and many geothermal sites host granitic rocks, such as the enhanced geothermal reservoirs of the Upper Rhine Graben (France) (Baria et al. 1999). Further, since granite is considered a major constituent of the continental crust (Wedepohl 1995), an understanding of time-dependent deformation in granite will assist in our understanding of crustal deformation and natural hazards. The stress distribution and permeability in a granite rock mass are important when we consider natural hazards and rock engineering projects. The distribution of stress (mechanical and thermal) dictates the microcrack anisotropy and therefore permeability anisotropy in granite (e.g., Sano et al. 1992; Benson et al. 2006; Nara et al. 2011a, b). However, and despite the importance of granite in these high-temperature environments, only few studies of time-dependent brittle creep on granite have been conducted at elevated temperature (Kranz et al. 1982; Lin et al. 2009; Chen et al. 2015; Wang et al. 2015).

During a brittle creep experiment, in which a rock sample is held at a constant differential stress for an extended period of time, the strain against time (the "creep curve") first decelerates before accelerating as macroscopic sample failure is approached, a behavior common to many rock types (Brantut et al. 2013). The onset of the acceleration to failure in brittle creep experiments has been ascribed as the result of the sample reaching a microcrack density at which microcracks can interact and coalesce, sometimes referred to as the "critical damage threshold" (Kranz and Scholz 1977; Baud and Meredith 1997; Heap et al. 2009b, 2011). The acceleration in strain rate during this accelerating phase has been previously described using a power law (Voight 1989).

Time-dependent brittle deformation is often attributed to a mechanism of subcritical crack growth called stress corrosion cracking (Atkinson 1984; Brantut et al. 2013). Stress corrosion describes fluid–rock reactions that occur preferentially between a chemically active pore fluid and strained atomic bonds at the crack tips and is therefore sensitive to environmental factors such as stress, temperature, and pore fluid reactivity (Atkinson 1984). Temperature influences the crack growth rate through the Arrhenius temperature dependence of crack growth rate (Heuze 1983) and because temperature affects the stress dependency of the rate of crack growth. Indeed, experimental work has shown that speed of crack growth during single crack double-torsion experiments is increased as temperature is increased (Meredith and Atkinson 1983; Nara et al. 2010, 2011a, b). Similarly, brittle creep experiments have shown that strain rates and time-to-failure are higher and lower, respectively, as temperature is increased (Kranz et al. 1982; Lockner 1993a, b; Heap et al. 2009a; Lin et al. 2009; Chen et al. 2015; Ye et al. 2015). For example, Kranz et al. (1982) observed a decrease in the time-to-failure in brittle creep experiments on granite by up to three orders of magnitude upon increasing sample temperature from 24 to 200 °C. Similarly, Heap et al. (2009a, b) experimentally observed an increase in creep strain rate of three orders of magnitude from 20 to 75 °C in experiments on sandstones. Ye et al. (2015) also found that high temperature (80 °C) reduced time-to-failure in brittle creep experiments on tuff. The enhanced rate of creep deformation is of particular interest in the context of nuclear waste disposal and geothermal energy.

Based on the experimental investigations, various creep models have been proposed over the last few decades which can be grouped into three classes: empirical models, component models, and mechanism-based constitutive models. Empirical models, based on laboratory investigations, are widely used in engineering (Cristescu 1993). However, due to the difference in timescale between laboratory investigations and the engineering project, the validation and suitability of these models for long-term predictions are dubious. Component models (Maranini and Yamaguchi 2001), which are generally a combination of standard elements such as the Newtonian dashpot, the Hooke spring, and the frictional element, have the advantage of a flexible description of the different creep deformations. The formulation of these models is always complex and often lacks physical meaning. In recent years, a mechanism-based creep model has been developed based on cracking and damage evolution at the microscale (Lockner and Madden 1991; Yoshida and Horii 1992; Shao et al. 1997; Amitrano and Helmstetter 2006; Lu et al. 2014); this type of model tries to build a bridge between macroscopic phenomenology and micromechanisms on a microscale (Shao et al. 2003, 2006; Bikong et al. 2015; Zhao et al. 2016).

Due to the aforementioned importance of understanding the long-term mechanical behavior of rock hosting nuclear waste disposal sites and geothermal reservoir rock, we present here a two-dimensional constitutive creep model to describe the time-dependent deformation of granite exposed to different temperatures and confining pressures. We also model the accompanying acoustic emissions (AEs), a diagnostic tool often used to monitor the progressive degradation of material at the mesoscale. We first formulate the thermo-mechanical coupled time-dependent model. We then validate the model and determine the required thermo-physico-mechanical properties using previously published experimental data (from Chen et al. 2015, 2017). Finally, we present and discuss the results of brittle creep simulations performed at different temperatures, differential stresses, confining pressures, and sample homogeneities.

2 Formulation of Time-Dependent Constitutive Model

The rapid advance of computer technology has enabled applied mathematicians, engineers, and scientists to make significant progress in the solution of previously intractable problems. Numerical modeling is currently the most commonly used method in the solution of important problems in rock mechanics and engineering. Thus, in this paper, a quantitative model is proposed to describe the coupled heat transfer and rock failure problems associated with rock exposed to elevated temperatures. To this end, a numerical thermo-mechanical creep code was developed to investigate time-dependent deformation at elevated temperature.

When formulating the model in mathematical language, various levels of complexity can be incorporated into each component, with the accuracy and versatility of the model depending on the refinement of the description of each component. For a model that can be used to investigate time-dependent creep deformation at high temperature, the coupled effect of the medium deformation and heat transfer must be important. Three components must be accounted for: (1) a heat transfer description, (2) a stress description, and (3) a failure description. The descriptions of heat transfer, stress, and failure in the model are, respectively, presented in this section.

The model is based on the theory of elastic damage mechanics and assumes that the damage is elastic and isotropic. The model accounts for material heterogeneity through a stochastic local failure stress field, and local material degradation using an exponential material softening

law. The maximum tensile strain criterion and a modified Mohr–Coulomb criterion with a tension cutoff are adopted as two failure thresholds in the model. The tensile strain criterion is preferential since the tensile strength of rock is commonly a tenth or twelfth of its compressive strength (Jeager et al. 2007). This approach makes it possible to simulate the transition from distributed damage by tensile microcracking to damage where microcracks can interact, coalesce, and ultimately form a throughgoing shear fracture. The model also describes the temporal and spatial evolution of AEs, including their size (energy released), in the medium during the progressive damage process.

Our approach differs from similar models, such as Amitrano and Helmstetter (2006), by accounting for heterogeneity by allowing the material strength and Young's modulus to follow a Weibull statistical distribution. Weibull distributions are often used in the field of failure analysis due to their flexibility and have been adopted by many researchers (Lajtai and Schmidtke 1986; Sornette et al. 1992; Tang 1997; Vázquez-Prada et al. 1999; Lu et al. 2002; Wong et al. 2006; Xu et al. 2012, 2013, Heap et al. 2016; Griffiths et al. 2017). Amitrano and Helmstetter (2006) introduced heterogeneity by assuming that the cohesions of the elements conform to a uniform distribution. Furthermore, our model can visually replicate the tempo-spatial evolution of the shear stress fields, the associated AE, and a rich assortment of other parameters, such as compressive stress, tensile stress, displacement vector, stress vector, and Young's modulus during the time-dependent brittle deformation of heterogeneous rock under a constant compressive stress, confining pressure, and temperature.

2.1 Characterization of Heterogeneity

In the absence of heterogeneity, the behavior of the model is entirely homogenous, no damage localization occurs, and the local behavior is replicated at the macroscopic scale. Thus, it is necessary to introduce heterogeneity to obtain a collective macroscopic behavior different from that of the individual elements. In order to reflect the material heterogeneity at a mesoscale, the mechanical parameters (e.g., strength and Young's modulus) of the mesoscopic material elements, which are assumed to be homogeneous and isotropic, are assigned randomly using a Weibull statistical distribution (Weibull 1951), as defined in the following statistical probability density function:

$$f(u) = \frac{\chi}{u_0} \left(\frac{u}{u_0} \right)^{\chi-1} \exp\left[-\left(\frac{u}{u_0} \right)^{\chi} \right] \tag{1}$$

where u is the scale parameter of an individual element such as the strength or Young's modulus and the scale parameter u_0 is related to the average element parameter. The shape parameter χ reflects the degree of material homogeneity and

is denoted as a homogeneity index. Figure 1 presents the statistical density distribution curves of uniaxial compressive strength of elements with a given scale parameter 100 MPa at different homogeneity indices ($\chi = 1.2, 1.5, 2, 3$ and 5). According to the Weibull distribution and the definition of homogeneity index as shown in Fig. 1, a larger χ implies that more elements will have the mechanical properties similar to the given scale parameter value, 100 MPa, resulting in a more homogeneous material.

To obtain a set of values of uniaxial compressive strength and Young's modulus following the Weibull statistic distribution, a set of random numbers ω_i ranging from 0 to 1 are generated based on the Monte Carlo method, and then, the uniaxial compressive strength and Young's modulus of each element can be obtained from:

$$u_i = u_0 \ln\left(\frac{1}{1 - \omega_i} \right)^{\frac{1}{\chi}} \tag{2}$$

where u_i is the uniaxial compressive strength and Young's modulus of the element i.

By randomly specifying a uniaxial compressive strength and Young's modulus to each of the elements, which follows the Weibull distribution according to Eq. (2), a heterogeneous numerical sample can be created. Figure 2 shows two numerical rock samples of 100 mm × 50 mm with a homogeneity index χ of 5 composed of twenty thousand (200×100) square elements. The uniaxial compressive strength (Fig. 2a) and the Young's modulus (Fig. 2b) are determined randomly according to the Weibull distribution (using a scale parameter of 350 MPa and 43 GPa for the strength and Young's modulus, respectively). The different colors in Fig. 2 correspond to different values of element strength and Young's modulus.
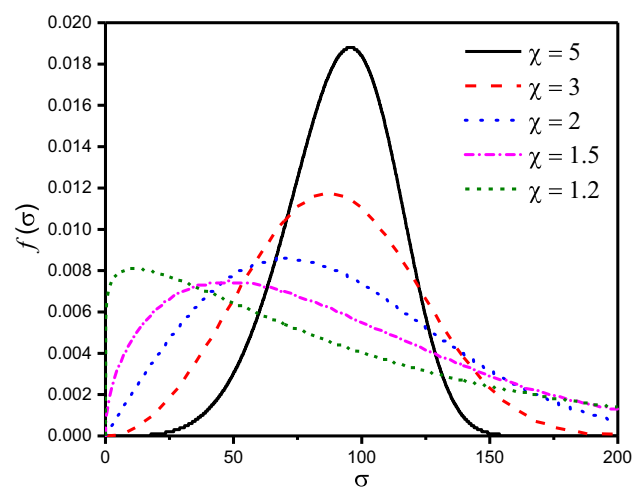

Fig. 1 Distribution density function of parameters of elements with different homogeneity indices χ ($\chi = 1.2, 1.5, 2, 3,$ and 5) at a given scale parameter of $u_0 = 100$
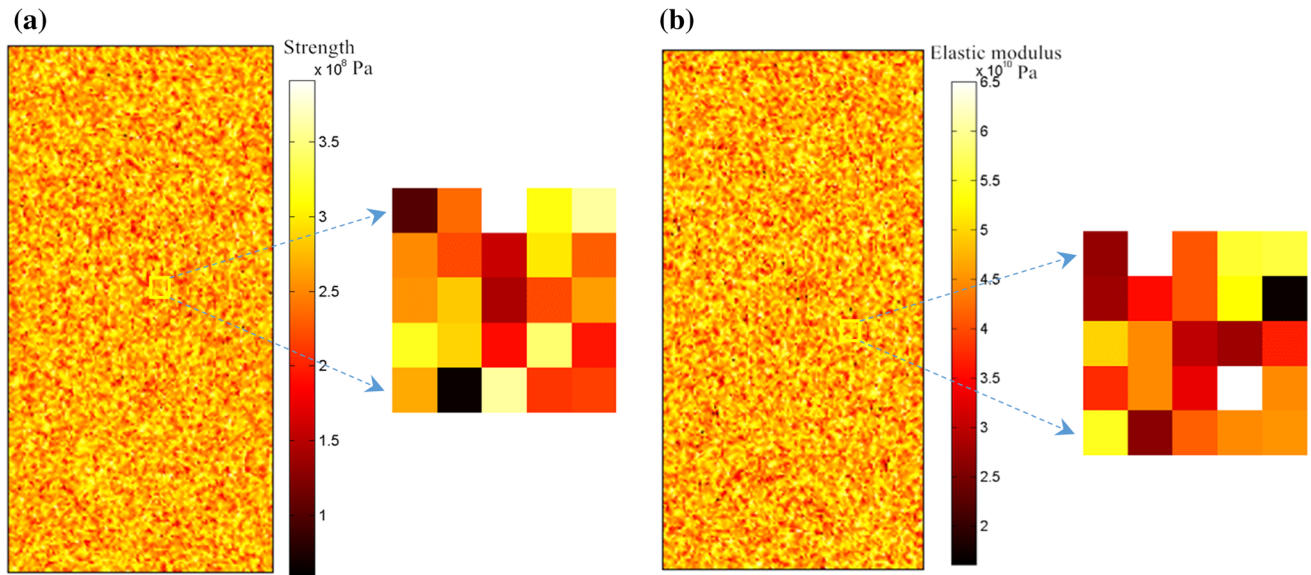
(a)

(b)

Fig. 2 Numerical specimens (100 mm in length and 50 mm in width) with a homogeneity index χ of 5. Each sample is composed of 20,000 elements. **a** The distribution of uniaxial compressive strength according to the Weibull distribution (scale parameter of 100 MPa) (see Eq. (1)). **b** The distribution of Young's modulus according to the Weibull distribution (scale parameter of 100 GPa) (see Eq. (1))

High values of χ lead to more homogeneous numerical samples, and vice versa. Therefore, the homogeneity index is an important parameter in controlling the macroscopic response of a numerical sample. Although a simplification, the differences in physical properties between different elements within a particular sample reflect differences in mineralogy (granite, for example, typically contains quartz, feldspar, and mica), cleavage or microcracks within individual crystals, crystal boundaries, among others.

2.2 Heat Transfer Description

Here we begin by considering the heat transfer description. The fundamental assumption behind the model presented here is that the conductive flux may saturate at a value comparable to the enthalpy per unit volume. Thermal conduction is defined as heat transport in a material by transfer of heat between portions of the material that are in direct contact with each other. The equation that governs the heat transfer in a medium is known as Fourier's Law:

$$q_i = -k_{ij}\text{grad}(T) \tag{3}$$

where q_i is the rate of heat conduction ($i = 1, 2, 3$) in W/m^2, k_{ij} is the apparent thermal conductivity tensor of the medium ($i, j = 1, 2, 3$) in W/m °C, and grad(T) is the temperature gradient in °C/m. The negative sign implies that heat is transferred in the direction of decreasing temperature. The thermal conductivity k varies between different materials and can be a function of temperature and temporal direction, but it can be treated as a constant for each element in the sample.

Assuming thermal equilibrium between the phases and heat conduction as the dominant mechanism of heat transfer, the energy balance equation in an anisotropic material can be expressed as:

$$\frac{\partial}{\partial x_i}\left(k_{ij}\frac{\partial T}{\partial x_j}\right) + q = \rho c \frac{\partial T}{\partial t} \tag{4}$$

where q denotes the heat source generated inside the medium in W/m^3, ρ is the bulk density of medium in kg/m^3, c is the specific heat or heat capacity of the medium in J/kg °C, and t is the time. For an isotropic material, the energy balance equation reduces to the following:

$$k\nabla^2 T + q = \rho c \frac{\partial T}{\partial t}. \tag{5}$$

2.3 Stress Description

It is assumed here that the total strain for a stressed medium is made up of elastic, creep, and thermal components. The total strain can therefore be decomposed as follows:

$$\varepsilon = \varepsilon_e + \varepsilon_c + \varepsilon_T \tag{6}$$

where the subscripts e, c, and T refer to the elastic strain, creep strain, and thermal strain, respectively. The elastic strain ε_e can be obtained using the tensor form of Hooke's law for elastic medium:

$$\varepsilon_e = \varepsilon_{ij} = \frac{1}{2G}S_{ij} + \frac{1}{3}\varepsilon_{kk}\delta_{ij} \tag{7}$$

where G is the shear modulus, ε_{ij} is the strain tensor form of the elastic strain ε_e, and S_{ij} is the stress deviator tensor of

the elastic stress components $\sigma_{ij}, S_{ij} = \sigma_{ij} - \frac{1}{3}\sigma_{kk}\delta_{ij}$, in which δ_{ij} is the Kronecker delta. The Kronecker delta equals zero when $i \neq j$ and one when $i = j$. The thermal strain ε_T is induced by thermal expansion due to the variation of temperature and can be expressed by:

$$\dot{\varepsilon}_{ij}^c = \frac{3}{2}AmS_{ij}\sigma_e^{n-1}t^{m-1}\exp\left(-\frac{U}{RT}\right) \tag{13}$$

where $\dot{\varepsilon}_{cij}$ is the creep strain rate, S_{ij} is the deviatoric part of σ_{ij}, and σ_e is effective stress defined as:

$$\sigma_e = \left(\frac{1}{\sqrt{2}}\right)\sqrt{(\sigma_{11} - \sigma_{22})^2 + (\sigma_{33} - \sigma_{22})^2 + (\sigma_{11} - \sigma_{33})^2 + 6(\sigma_{12}^2 + \sigma_{23}^2 + \sigma_{13}^2)} \tag{14}$$

$$\varepsilon_T = \alpha\Delta T\delta_{ij} \tag{8}$$

where α is the coefficient of linear thermal expansion and ΔT is the temperature change. The creep strain ε_c is a function of the stress σ, temperature T, and time t, i.e., $\varepsilon_c = F(\sigma, T, t)$. It is customary to assume that the effects are separable and can be written as:

$$\varepsilon_c = f(\sigma)g(T)h(t) \tag{9}$$

where $f(\sigma)$, $g(T)$, and $h(t)$ are the functions related to stress, temperature, and time, respectively.

For creep problems, a Norton–Bailey equation (Heard 1976; Carter and Hansen 1983) known as a constitutive law of the creep strain rate was adopted to characterize time-dependent creep deformation based on the approach of the equation of state theory:

$$\varepsilon_c = A\sigma^n t^m \exp\left(-\frac{U}{RT}\right) \tag{10}$$

where A, m, n are constants that are a function of temperature. The constant n usually denotes stress component and is greater than one; m is usually a fraction; U is the creep activation energy that can be determined empirically as proportional to the slope of a plot of $\log \varepsilon_c$ as a function of $1/T$ at constant σ, R is the universal gas constant, and T is the absolute temperature (in Kelvin).

Since modeling the strain rate is of great interest for this study, Eq. (10) can also be expressed in a strain rate form:

$$\dot{\varepsilon}_c = mA\sigma^n t^{m-1}\exp\left(-\frac{U}{RT}\right) \tag{11}$$

Since creep flow rule can be expressed in tensor form under multi-axial stress conditions (Kraus 1980):

$$\dot{\varepsilon}_{ij}^c = \frac{3}{2}\frac{d\bar{\varepsilon}_c}{dt}\frac{S_{ij}}{\sigma_e} \tag{12}$$

in which σ_e is the effective stress and $\sigma_e = \sqrt{\frac{3}{2}S_{ij}S_{ij}}$, $d\bar{\varepsilon}_c$ is the effective creep strain, and $d\bar{\varepsilon}_c = \sqrt{\frac{2}{3}d\varepsilon_{ij}^c d\varepsilon_{ij}^c}$. Now, substitute Eq. (12) into Eq. (11), the creep strain rate is also extended to the multi-axial stress case:

This creep model can describe the decelerating creep commonly seen at the start of a brittle creep experiment (e.g., see Brantut et al. 2013), but it fails to represent the acceleration in strain rate in the approach to macroscopic sample failure. Thus, a damage evolution law for the accelerating creep of rock is incorporated at this stage.

The description of stress can be formulated in a number of ways. The static stress equilibrium equation for macroscopic total stresses in the absence of an inertia term takes the form:

$$\sigma_{ij,j} + f_i = 0 \tag{15}$$

where σ_{ij} is the total stress tensor ($i, j = 1, 2, 3$) in MPa and f_i is the body force per unit volume in MPa. According to the continuous conditions, for a perfectly elastic isotropic continuum, the continuity equation is expressed in terms of the displacement gradient:

$$\varepsilon_{ij} = \frac{1}{2}\left(u_{i,j} + u_{j,i}\right) \tag{16}$$

where $\varepsilon_{i,j}$ is small strain tensor ($i, j = 1, 2, 3$), and u is the displacement of the medium. The constitutive equation of deformation fields for elastic isotropic medium can be expressed as:

$$\sigma_{ij} = \lambda\delta_{ij}\varepsilon_{ii} + 2G\varepsilon_{ij} - \beta\delta_{ij}\Delta T \tag{17}$$

where G is shear modulus, λ is Lamé's constant, β is the coefficient of thermal stress in 1/°C, and $\beta = (3\lambda + 2G)\alpha$. Based on the theory presented above, the static stress equilibrium equation, the continuity equation, and the constitutive equations, the final governing equation of heat transfer in a medium can be written in displacement form as follows:

$$(\lambda + G) \cdot u_{j,ji} + Gu_{i,jj} + f_i - \beta\delta_{ij}\Delta T = 0 \tag{18}$$

2.4 Damage Evolution Description

Damage mechanics is concerned with the representation or modeling of damage of materials. This approach is suitable for making engineering predictions about the initiation, propagation, and fracture of materials without

resorting to a microscopic description that would be too complex for practical engineering analysis (Krajcinovic 2000; Lemaitre and Desmorat 2005). Damage mechanics is a commonly used approach in engineering to model complex phenomena. It has been widely adopted in the study of damage of various materials, such as metal-based materials (Khelifa et al. 2007), biomaterials (Zitnay et al. 2017), composites (Yang and Cox 2005), and quasi-brittle materials (Zhu and Shao 2015; Qi et al. 2016). In the model used herein, the theory of damage mechanics is also adopted and the system is analyzed at the mesoscale and an elastic damage constitutive law can describe its stress–strain relationship. Continuum damage mechanics can describe the effects of progressive microcracking, void nucleation, and microcrack growth at high stress levels using a constitutive law, by making use of a set of state variables modifying the material behavior at the macroscopic level. Using an isotropic continuum damage formulation, the elastic modulus for an isotropic and elastic medium at instantaneous loading can be written as (Lemaitre and Desmorat 2005):

$$E = E_0(1 - D) \tag{19}$$

where ε_{ij} is the damaged elastic strain tensor, σ_{ij} is the stress tensor, E and E_0 are the Young's moduli of the damaged and the undamaged material, respectively, D is the isotropic damage variable, v is the Poisson's ratio and δ_{ij} is the Kronecker symbol. In the case of a uniaxial state of stress ($\sigma_{11} \neq 0, \sigma_{22} = \sigma_{33} = 0$), the constitutive relation can be rewritten in terms of the longitudinal stress and strain components only:

$$\sigma_{11} = E_0(1 - D)\varepsilon_{11} \tag{20}$$

Hence, for uniaxial loading, the constitutive law is explicitly dependent on damage index D.

The model is based on progressive isotropic elastic damage. When the stress on an element exceeds a damage threshold, its Young's modulus E is modified according to Eq. (19). At the beginning, each element is considered to be elastic, defined by a specific Young's modulus and Poisson's ratio. The stress–strain curve of the element is considered linear elastic with a constant residual strength until the given damage threshold is reached. This proceeded by a phase of softening.

The elastic damage constitutive law of each element under uniaxial stress condition is illustrated in Fig. 3 (Zhu et al. 2014). The stress–strain curve of each element is considered linear elastic until the given damage threshold is attained. We choose the maximum tensile stress criterion and modified Mohr–Coulomb criterion as the damage thresholds to determine whether any elements are damaged in tension or shear, respectively, which are expressed as:
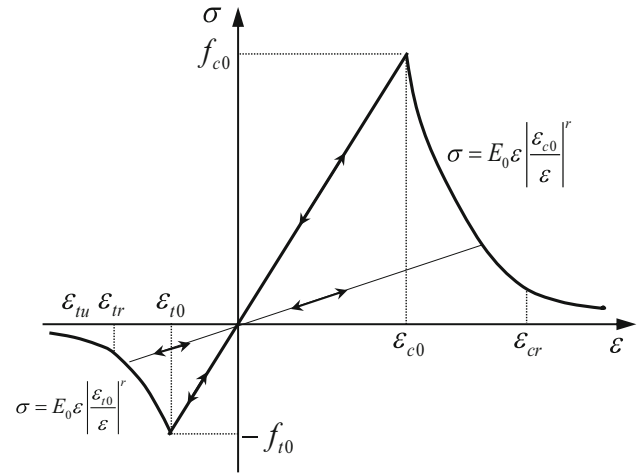

Fig. 3 Elastic damage constitutive law for element under uniaxial compression and tension

$$F_1 = -\sigma_3 - f_{t0} = 0 \quad \text{and}$$
$$F_2 \equiv \sigma_1 - \sigma_3 \frac{1 + \sin\varphi}{1 - \sin\varphi} - f_{c0} = 0 \tag{21}$$

where σ_1 and σ_3 are the maximum and minimum principal stresses, respectively, f_{c0} is the uniaxial compressive strength, ϕ is the internal friction angle of the element, f_{t0} is the uniaxial tensile strength, and F_1 and F_2 are two damage threshold functions. The tensile strain criterion is always used with priority to judge whether the element is damaged or not. If the element is not damaged in tension, the Mohr–Coulomb criterion is then used to judge whether the element is damaged in shear. The sign convention used throughout this paper is that compressive stresses are positive and tensile stresses are negative.

According to the constitutive law as shown in Fig. 3, the damage variable D can be described as follows:

$$D = \begin{cases} 0 & F_1 < 0 \quad \text{and} \quad F_2 < 0 \\ 1 - \left|\frac{\varepsilon_{t0}}{\varepsilon_1}\right|^r & F_1 = 0 \quad \text{and} \quad \mathrm{d}F_1 > 0 \\ 1 - \left|\frac{\varepsilon_{c0}}{\varepsilon_3}\right|^r & F_2 < 0 \quad \text{and} \quad \mathrm{d}F_2 > 0 \end{cases} \tag{22}$$

where ε_1 and ε_3 are major principal strain and minor principal stain, respectively. ε_{t0} and ε_{c0} are the maximum principal strain in tension and the maximum principal strain in compression when damage occurs according to the maximum tensile stress criterion and Mohr–Coulomb criterion, respectively, and r is a constitutive coefficient with a value of 2. We highlight that the element will behave elastically during loading and unloading when the main tensile strain or the main compressive strain of the element is less than the maximum principal strain in tension and the maximum principal strain in compression, respectively (see Fig. 3). When either of these strain thresholds is exceeded,

the element will be damaged and the behavior can be described, during loading or unloading, by Eq. (22).

The damage variable calculated with Eq. (22) is always from 0 to 1, regardless of the type of damage (tensile or shear). However, in the damage zone, in order to distinctly display the two kinds of damage modes (i.e., tension and shear) in the post-processing figures, tensile damage is represented as negative numbers, while the shear damage is represented as positive ones. During the numerical implementation of the above equations with finite element analysis, Eq. (21) was used as a damage criterion to check the stress conditions calculated with Eqs. (6) and (13) in order to judge whether damage occurs or not. Thus, Eq. (22) was used to calculate the damage variable *D*. If any elements are damaged in the stressed specimen, the damaged elements will undergo degradation of their elastic modulus according to the elastic damage constitutive relationship. In this model, $D = 1$ means the complete failure of the element, and elastic modulus of the element tends to zero. In order to avoid possible instability in finite element analysis, a small decimal (1.0×10^{-5} MPa by default) is specified to the elastic modulus of a failed element. Correspondingly, total strain will increase due to the elastic modulus degradation and increasing time. When damaged or failed elements are clustered, it may lead to the acceleration in strain rate that precedes macroscopic failure. Therefore, although Eq. (22) is time-independent, it can be capable of describing the time-dependent evolution of damage when it is coupled with the creep model given in Eq. (13) to describe the creep behavior of rock.

AEs are transient elastic waves generated by the rapid release of energy within a material, such as the strain energy released during microcrack propagation. Monitoring AE during deformation has become an increasingly important diagnostic tool in material science and has provided a wealth of information regarding the failure process in brittle materials. AE monitoring has, for example, shed light on the onset of inelastic damage during deformation (Wong et al. 1997) as well as its spatial and temporal evolution (Ohnaka 1983; Lockner 1993a, b; Townend et al. 2008; Fortin et al. 2009; Aker et al. 2014; Heap et al. 2015). For instance, Lockner (1993a, b) analyzed catalogues of AE events recorded during compressive loading tests on rock. The events were analyzed in terms of the information they offer about the accumulated state of damage in a material. This measured damage state can be combined with a model for the weakening behavior of cracked solids, showing that reasonable predictions of the mechanical behavior are possible. Based on this prior knowledge, it is reasonable to assume that the number of AE events is proportional to the number of damaged elements and that the strain energy released (the strain energy before and after damage) corresponds to the energy of that

particular AE event (Tang 1997). In our model, we can use the output of AE to indirectly assess the damage evolution. However, it must be mentioned that aseismic damage during rock creep tests could possibly occur, and subcritical micromechanisms other than stress corrosion, such as pressure solution, may become important (Brantut et al. 2014). The causes of aseismic damage are numerous, for example: the low surface energy of calcite, radiated energy being absorbed by neighboring dislocation, and/or intermittent dislocation flow (Weiss and Marsan 2003; Schubnel et al. 2006). Although this approximation is obviously a simplification of what occurs in reality, it has been shown that this micromechanical representation of microcracking can yield realistic patterns and can reproduce the macromechanical behavior of heterogeneous rock.

The cumulative damage, ψ, in a given volume of rock, due to local failures can be defined as the ratio of the volume of failed rock, V_f, to the total volume, V:

$$\psi = \frac{V_f}{V} = \frac{v_e \cdot \sum_1^s n_i}{N \cdot v_e} = \frac{1}{N} \sum_1^s n_i \tag{23}$$

where v_e is the volume of single element, s is the number of calculation steps, n_i is the number of failed elements in the *i*th step, and N is the total number of elements in the model. For a perfectly elastic brittle material, the energy e_f released by the failure of each element can be calculated from the element peak strength:

$$e_f = \frac{\sigma_0^2}{2E_0} + \int f(\sigma, \varepsilon - \varepsilon_0) d(\varepsilon - \varepsilon_0) v_e \tag{24}$$

where σ_0 is the peak strength of the element and E is the Young's modulus of the element. The cumulative seismic energy can then be obtained by:

$$\sum e_f = \sum \left(\frac{\sigma_0^2}{2E} + \int f(\sigma, \varepsilon - \varepsilon_0) d(\varepsilon - \varepsilon_0) v_e \right) \tag{25}$$

Thus, by recording the number of failed elements, the AE associated with the progressive failure of the material can be simulated in our model.

In the numerical code, for a given numerical model, the numerical model is loaded either in a displacement control mode (i.e., constant displacement rate) or in a load control mode (i.e., constant stress). At each loading or time increment, the stress and strain, and the coefficient of thermal conductivity in the elements are calculated, then the stress field and flow field are examined, and those elements that are strained beyond the pre-defined strength threshold level are broken irreversibly. To break an element means to reduce the element stiffness and its strength, and at the same time, the coefficient of thermal conductivity also changes with the stress. If some elements fail, then the model, now containing new parameters for some of its elements, moves

to a new equilibrium. The next load or time increment is added only when there are no more elements strained beyond the strength threshold level at an equilibrium strain field. Thus, numerical loading in the model is similar to that of deformation experiments performed in the laboratory.

2.5 Boundary conditions

Equations (5), (6), (11), (18), (19), and (22) represent governing equations for the coupled thermal–mechanical damage time-dependent model which are numerically solved using finite element method. The unknowns are displacement and temperature. Generalized initial displacement and thermal conditions are:

Displacement: $U(x, y, t) = U(x, y, 0)$, on B
Thermal: $T(x, y, t) = T(x, y, 0)$, on B

where (x, y) represents a position vector, t represents time, and U and T are the known displacement and temperature, respectively. B denotes the continuum region enclosed by a boundary. The following generalized boundary conditions are set for the numerical computation:

Displacement: $U_i(x, y, t) = \widehat{U}_i(x, y, 0)$, on B_u
Traction: $\sigma_{ij}(x, y, t) \cdot n_j = \widehat{\sigma_{ij}}(x, y, 0)$, on B_σ

For the boundary conditions on the medium, it can be of Dirichlet type, where the temperature on the boundary is specified, that is:

$$T|_s = T_b(B, t), \quad (B \in S_1, t > t_0). \tag{26}$$

It can also be of Neumann type where the heat flux is specified:

$$
\begin{aligned}
q_n|_s &= -k \frac{\partial T}{\partial n}\Big|_s \\
&= q_b(B, t), \quad (B \in s_2, t > t_0).
\end{aligned}
\tag{27}
$$

A generalized Neumann boundary condition can also be used. The generalized Neumann boundary condition equation is written as:

$$
\begin{aligned}
q_n|_s &= -k \frac{\partial T}{\partial n}\Big|_s \\
&= h(T - T_a), \quad (B \in s_3, t > t_0)
\end{aligned}
\tag{28}
$$

where h is the rock/fluid convective heat transfer coefficient in W/m^2 °C, and the T_a is the ambient temperature.

3 Implementation of Numerical Model

The modeling approach described above requires that both the damage state and the damage-induced alteration of elastic stiffness in brittle rocks be continually updated with an increase in the applied stress induced by external constant load or temperature, and the progression of time. Consequently, this problem is highly nonlinear. An iterative numerical procedure is implemented for this model that is based on the finite element method. A flow chart of the model is shown in Fig. 4 to clarify the implementation of the numerical model. The procedure outlined in Fig. 4 is first performed in MATLAB to define the evolution of the damage constitutive parameters and then implemented into the finite element model COMSOL Multiphysics to define spatial behavior.

A point worth emphasizing here is that the proposed model needs to be first calibrated with experimental data to determine appropriate input parameters. In principle, a complete calibration process must be undertaken at both the mesoscale and the macroscale. At the mesoscale, the behavior of the REV (representative elemental volume) is governed by the initial microstructural parameters, the damage-based constitutive law, and the failure criterion of the REV. It is straightforward to obtain accurate parameters to represent the initial mesoscale structures in the REV from mesoscopic observations, but the calibration of the damage constitutive law and the failure criterion at the mesoscale is more challenging—principally due to the difficulties in performing direct mechanical tests on the REV. An approximate method is the utilization of macroscopic standard laboratory tests instead of mesoscopic tests (Homand-Etienne et al. 1998). However, the development of novel experiments at the mesoscale of the REV is needed to further improve model calibration at the mesoscale. With the calibrated mesoscale parameters defined, then the macroscopic numerical model can be calibrated from conventional compression tests and creep tests on standard rock samples to determine the parameters of heterogeneity and REV size. After the full calibration of the proposed model, it can be used to predict the time-dependent deformation and fracturing behavior of brittle rocks at elevated temperature.

Currently, a few calibration studies partially related to our proposed model have been performed on different types of rocks (Golshani et al. 2006; Wong et al. 2006). In the following, the input model parameters are chosen referring to these calibrated parameters. However, further studies must explore more accurate and rigorous model calibration with new experiments conducted on the same type of rock samples at both the meso- and macroscale. In the following section, the model is first validated against previously published experimental data to obtain the input parameters for the simulations. Then, our model is used to simulate the time-dependent brittle creep behavior of rocks under uniaxial and triaxial loading conditions at various constant temperatures.

Fig. 4 Flow chart of the coupled numerical model
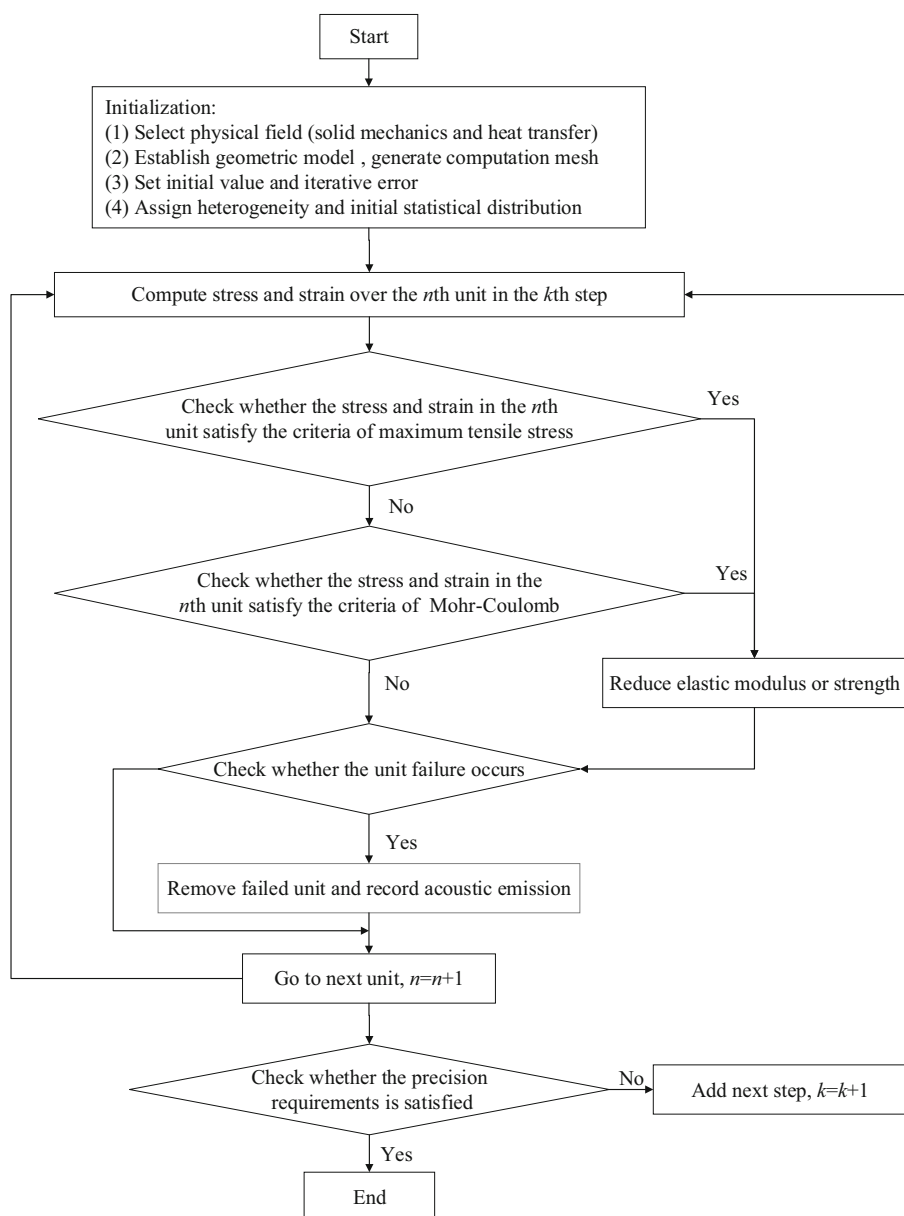
4 Validation of the Model

Before we can investigate the influence of various parameters on brittle creep (such as temperature, differential stress, confining pressure, and sample heterogeneity), we must first validate our model using previously published experimental data. To do so, we use recently published data (Chen et al. 2015, 2017) on low-porosity Beishan granite (described in detail below). Importantly for our validation, these experiments cover a range of experimental conditions (different confining pressures and temperatures) and loading configurations (constant strain rate and constant stress). We highlight that our model is two dimensional, and the experiments of Chen et al. (2017) are conducted on

cylindrical samples. Nevertheless, we consider our two-dimensional model to be a reasonable approximation of the three-dimensional case.

4.1 Presentation of Beishan Granite

Based on the range of available experimental data, and because the Beishan site is a potential site for a high-level radioactive waste repository in China, we have chosen to study Beishan granite. The macroscopic mechanical properties of Beishan granite have been investigated and described in previous studies (Chen et al. 2012, 2014, 2015, 2017; Zhao et al. 2013; Zong et al. 2013). Beishan granite is a fine- to medium-grained granite

(crystal diameter varies from a couple of hundred microns up to a few mm) that contains a porosity of 0.4%. It consists of 52% plagioclase, 17% quartz, 15% alkali feldspar, 12% biotite, 3% albite, and <1% myrmekite (Zhao et al. 2013).

4.2 Constant Strain Rate Experiments

We used mechanical data from constant displacement rate uniaxial and triaxial experiments performed at room temperature to obtain the physico-mechanical input parameters at the mesoscale. The geometry of the granite samples in laboratory experiments used here was 100 mm in length and 50 mm in width (data from Chen et al. 2015). The unconfined compressive strength of air-dried Beishan granite is 165.2 MPa, and the compressive strength of air-dried Beishan granite under confining pressures of 1 and 5 MPa are 174 and 216.8 MPa, respectively (Chen et al. 2015) (Fig. 5). The Young's modulus and Poisson's ratio of air-dried Beishan granite in uniaxial compression are 43 GPa and 0.25 (Chen et al. 2015). As for the experimental tests in laboratory, numerical specimens 100 mm in length and 50 mm in width were prepared. These numerical samples were randomly generated and discretized into 200×100 (20,000 elements) square elements (i.e., each square element had sides of 0.5 mm). The size of the modeled sample kept the same for all of the numerical simulations throughout this paper. A suite of prescribed displacement increments were uniaxially applied to both ends of the modeled rock samples at constant room temperature and constant confining pressures of 0, 1, and 5 MPa. During the simulations, the elements within the modeled rock sample are fixed in the vertical direction but can move freely in the horizontal direction, as is the case for axial compressive loading in the laboratory. The modeled samples were then loaded under a constant displacement rate. The best-fit physico-mechanical input parameters of the individual elements at a mesoscale used in the simulations were determined by trial-and-error (Table 1). It is noted that the input parameters for the elements at a mesoscale listed in Table 1 represent the statistical mechanical properties of the granite specimen at a macroscale.

The numerical stress–strain curves for the granite simulations, together with the experimental stress–strain curves from the published experimental data of Chen et al. (2015), are plotted in Fig. 5. Figure 5 shows that the simulated stress–strain curves are in good agreement with the experimental stress–strain curves. The nonlinear behavior at the beginning of the experimental stress–strain curves is a result of the closure of pre-existing compliant microcracks (Fig. 5). This nonlinearity is not replicated in the model because the stress–strain behavior of an element is considered linear elastic until the given damage threshold is attained. Importantly, we highlight that the model input
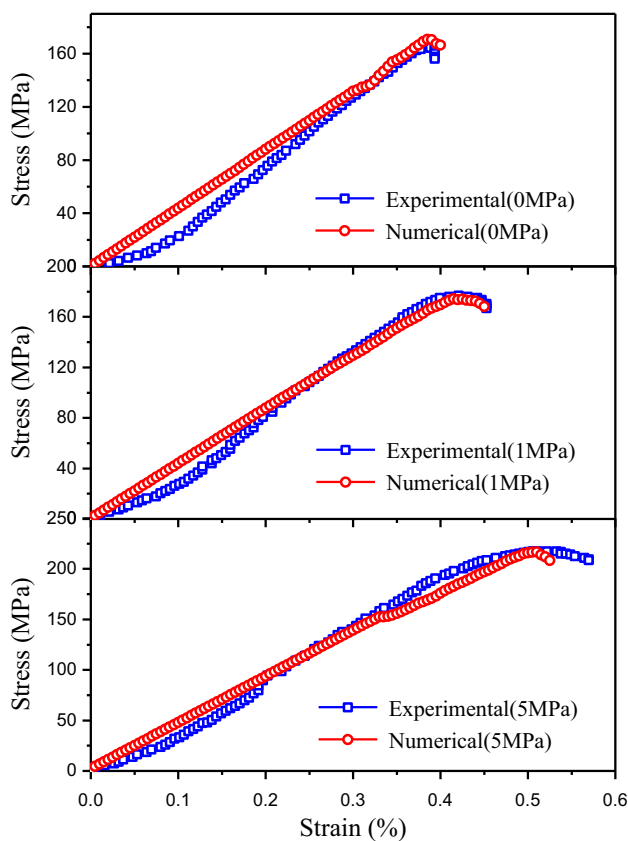

Fig. 5 Comparison between numerical (*red circles*) and experimental (*blue squares*; data from Chen et al. 2015) stress–strain curves for granite samples in compression. Values in MPa on each panel refers to the confining pressure (σ_x) (color figure online)

Table 1 Thermo-physico-mechanical parameters of the numerical model

Parameter	Beishan granite
Homogeneity index χ	5
Mean Young' modulus (GPa)	43
Mean UCS (MPa)	350
Poisson ratio	0.25
Ratio of compressive to tensile strength	10
Frictional angle (°)	30
Prescribed constant stress (MPa)	150
Specific heat capacity (J/kg K)	900
Coefficient of linear thermal expansion (1/K)	4.6×10^{-6}
Thermal conductivity (W/m K)	3.48
A	6.8×10^{-11}
n	1.75
m	0.39
U	3000

parameters were the same for each of the simulations shown in Fig. 5 (Table 1), adding confidence that the model is capable of accurately capturing the short-term mechanical behavior of Beishan granite under different confining pressures.

4.3 Conventional Brittle Creep Experiments

The validity of our numerical model was tested via a successful attempt to replicate previously published uni-axial and triaxial experimental data for air-dried Beishan granite (Fig. 5) (Chen et al. 2015). We will now model a suite of conventional brittle creep experiments on air-dried Beishan granite under different constant temperatures of 23, 50, and 90 °C in order to find the required thermo-physico-mechanical properties of the granite, such as specific heat capacity, coefficient of linear thermal expansion, and thermal conductivity. Importantly, we use here the same physico-mechanical input parameters as for the simulations presented in the previous section (listed in Table 1). The temperatures of 23, 50, and 90 °C, respectively, represent room temperature, the in situ rock temperature, and the maximum temperature on the canister surface according to the current nuclear waste disposal concept in China. Similar to laboratory creep experiments (Chen et al. 2015), the numerical brittle creep simulations consisted of two stages: (1) an initial loading stage, where the sample is loaded to a pre-determined level of stress, and (2) a constant stress and constant temperature stage, where the sample is kept at a constant stress and a given constant temperature until macroscopic sample failure or until it was clear that the sample would not fail under the imposed constant stress in a reasonable time period.

The uniaxial numerical creep simulations were all performed using the determined physico-mechanical parameters listed in Table 1 and under constant temperatures of 23, 50, and 90 °C. To simulate time-dependent behavior at elevated temperature, the thermo-physical parameters such as specific heat capacity, coefficient of linear thermal expansion, and thermal conductivity, as well as the material constants A, m, and n, are required. Based on the experimental data on macroscopic physico-mechanical properties of rocks, and the statistical distribution relationship between the physico-mechanical properties of the elements at the mesoscale and the phy-sico-mechanical properties of rocks at a macroscale, the thermo-physico-mechanical properties of the elements at the mesoscale can be determined using an inverse analysis method. Thus, these thermo-physical parameters were determined from the experimental data (Chen et al. 2015), and material constants A, m, and n can be determined using a fitting method. All of the input parameters for the numerical model are listed in Table 1. Our determined

values of thermal properties are within the range expected for granite (Clauser and Huenges 1995). For example, our thermal conductivity value of 3.48 W/m K (Table 1) is within the range of values found for granite from the Soultz-sous-Forêts geothermal site in France (2.3–3.9 W/m K) (Surma and Geraud 2003). During the simulations, the elements in the modeled rock sample are fixed in the vertical direction, but they can move freely in the horizontal direction, as is the case for axial compressive loading in the laboratory.

The numerically simulated creep curves (axial strain as a function of time), together with the experimental creep curves (Chen et al. 2015), are plotted in Fig. 6. Figure 6 shows that the simulated creep curves are in good agreement with the experimental curves. The numerical creep curves produced by our model clearly capture the phenomenology of brittle creep: the strain rate first decelerates, followed by an acceleration in strain rate prior to macroscopic failure (Fig. 6). In detail, the time-to-failure and the strain at the onset of acceleration to failure are very similar between the simulations and the experiments (Fig. 6).

Figure 7 shows several snapshots of the damage evolution of the numerical specimens deformed at constant temperatures of 23, 50, and 90 °C (the same simulations shown in Fig. 6). The snapshots of Fig. 7 show when and where damage and failure occur in the numerical specimen. Because the numerical rock samples are heterogeneous, the value of Young's modulus is randomly distributed. There are therefore many elements that have a low Young's modulus; these elements act as nucleation sites for damage. As time goes on, these damaged units grow and form localized damage zones. The localized damaged zones modify the stress field in their surrounding region, and these modifications further trigger the dynamic extension of the damage zone. Eventually, a throughgoing fracture forms that signals the macroscopic failure of the sample, as shown in the final snapshot for each experiment (Fig. 7).

4.4 Multi-Step Brittle Creep Experiments

Recently, Chen et al. (2017) performed a series of uniaxial and triaxial multi-step creep experiments to investigate the influence of temperature and stress on the time-dependent behavior of air-dried Beishan granite. Multi-step creep tests were conducted at various constant confining pressures of 0, 1, and 5 MPa and at temperatures of 23 (room temperature) and 90 °C (the maximum temperature on the canister surface according the current disposal conceptual design in China), respectively. During the multi-step creep experiments (Chen et al. 2017), the stress applied on the sample was increased stepwise to pre-determined percentages of the average peak stress (20, 40, 60, and 80%). The sample was kept at each level of stress for one week. To further
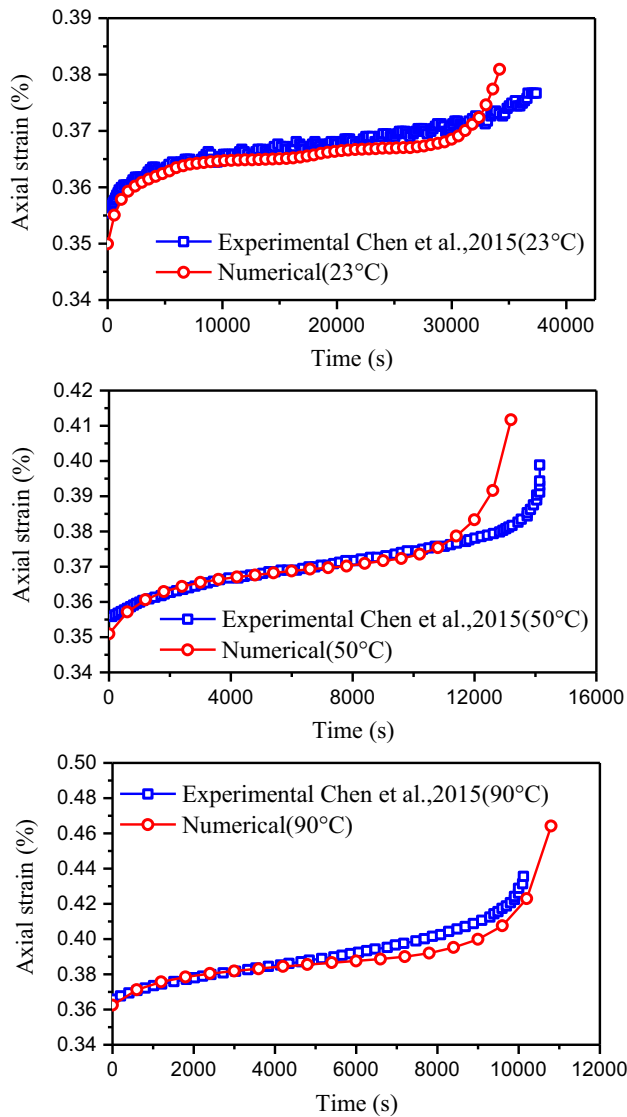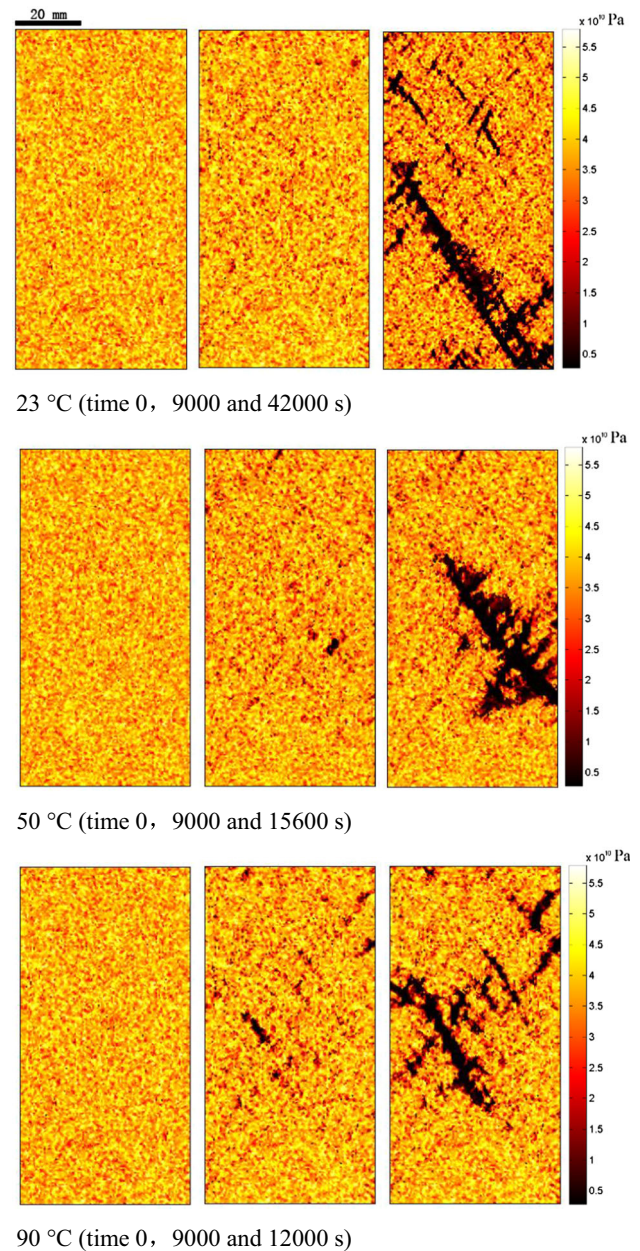
Fig. 6 Creep curves (axial strain as a function of time) for simulations performed under uniaxial conditions ($\sigma_x = 0$ MPa) at constant temperatures of 23, 50, and 90 °C (*red circles*), together with experimental data from Chen et al. (2015) under the same conditions (*blue squares*). All simulations and experiments were performed under the same constant differential stress ($\sigma_y = 150$ MPa) (color figure online)

23 °C (time 0，9000 and 42000 s)

50 °C (time 0，9000 and 15600 s)

90 °C (time 0，9000 and 12000 s)

Fig. 7 Snapshots of the failure process during the brittle creep simulations shown in Fig. 7. All simulations were performed under uniaxial conditions ($\sigma_x = 0$ MPa) and under the same constant differential stress ($\sigma_y = 150$ MPa)

validate our model, we performed numerical multi-step creep simulations under the same conditions. Importantly, the numerical multi-step creep simulations were all performed using the determined physico-mechanical and thermo-physical parameters listed in Table 1. During the simulations, the elements in the modeled rock sample are fixed in the vertical direction, but they can move freely in the horizontal direction, as is the case for axial compressive loading in the laboratory.

The numerically simulated multi-step creep curves (axial strain as a function of time), together with the experimental multi-step creep curves (Chen et al. 2017), are plotted in Fig. 8. Figure 8 shows that the simulated

multi-step creep curves are in good agreement with the experimental curves. In detail, the model captures the influence of both confining pressure and temperature on the mechanical behavior, and the strain at the different stress steps and the time-to-failure are very similar between the experiment and the model (Fig. 8).

We therefore conclude that, based on the above validations, our model can be used to investigate time-dependent creep of low-porosity granite at different temperatures. We will now use our model to further
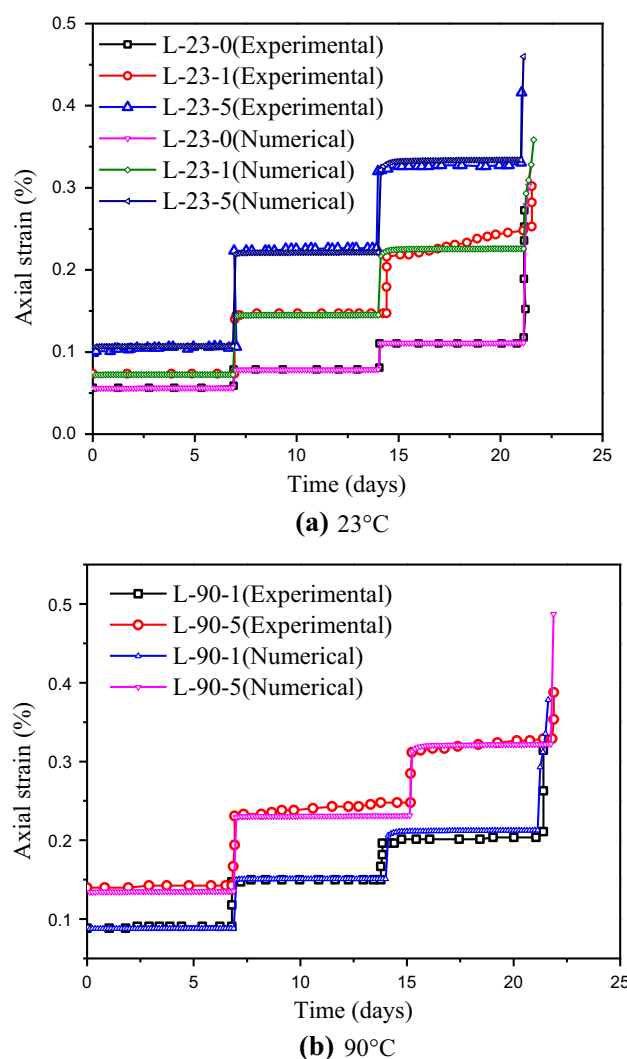
(a) 23°C

(b) 90°C

Fig. 8 Multi-step creep curves (axial strain as a function of time) for simulations performed under different confining pressures ($\sigma_x = 0$, 1, and 5 MPa) and temperatures (23 and 90 °C), together with experimental data from Chen et al. (2017) under the same conditions

explore the influence of temperature, differential stress, confining pressure, and sample heterogeneity on brittle creep in low-porosity granite.

5 Numerical Simulations and Discussion

5.1 Model Setup

In this section, we use the proposed model to further investigate the influence of temperature, differential stress, confining pressure, and sample heterogeneity on brittle creep of low-porosity granite. Our numerical samples have a geometry of 100 mm × 50 mm (Fig. 9), the same as the samples modeled in the validation described above. The geometry of the modeled samples was discretized into a
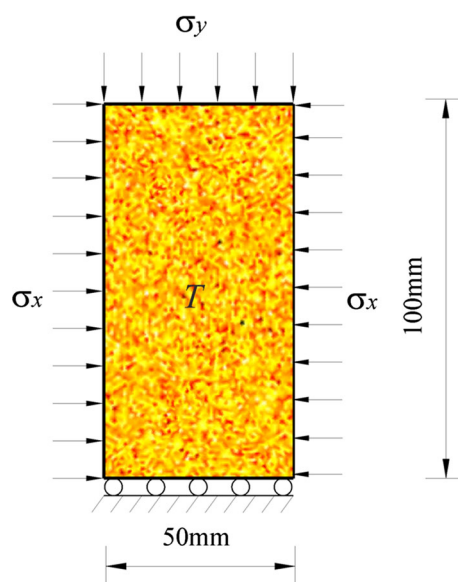
Fig. 9 Model geometry and loading conditions for the simulated creep experiments. T—temperature, σ_y—axial stress, and σ_x—confining pressure

200×100 (20,000 elements) square grid (i.e., each square element had sides of 0.5 mm). We applied various axial stresses (140, 145, 150, 155, and 160 MPa), and various constant temperatures (23, 40, 50, 75, and 90 °C) on numerical heterogeneous samples ($\chi = 4$, 5, and 6), respectively, to investigate the influence of temperature, differential stress, and sample heterogeneity on brittle creep in granite. The loading conditions are also shown in Fig. 9. Similar to conventional creep tests, the axial stress (σ_y) was maintained constant at the top of the specimen. At the same time, a constant confining pressure (σ_x) was maintained on the sample (this pressure was set at 0 MPa for uniaxial simulations), and the temperature was held constant during the simulations. During the simulations, the elements within the modeled rock samples are fixed in the vertical direction but can move freely in the horizontal direction, as is the case for axial compressive creep experiments in the laboratory. The relevant model parameters used in the simulations are the same as the parameters listed in Table 1.

5.2 Effect of Temperature

Based on the validations above, two additional brittle creep simulations were performed under uniaxial compressive loading conditions ($\sigma_y = 150$ MPa) at constant temperatures of 40 and 75 °C. The resulting creep curves (axial strain as a function of time) for various constant temperatures (23, 40, 50, 75, and 90 °C) are presented in Fig. 10. The creep curves presented in Fig. 10 clearly show the accelerating–decelerating phenomenology of brittle creep
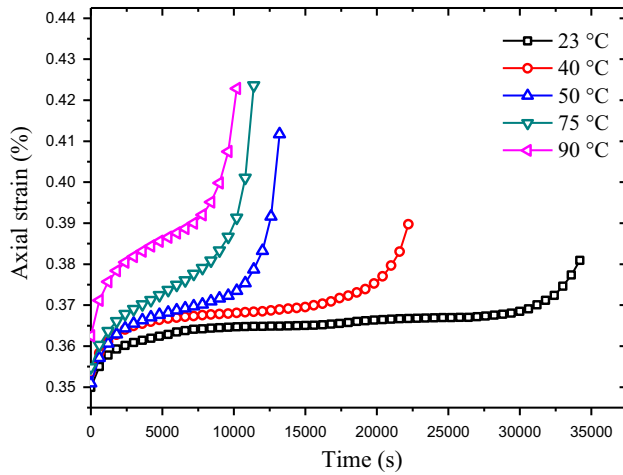
Fig. 10 Creep curves (axial strain as a function of time) for simulations performed under uniaxial conditions ($\sigma_x = 0$ MPa) at constant temperatures of 23, 40, 50, 75, and 90 °C. All simulations were performed under the same constant differential stress ($\sigma_y = 150$ MPa)
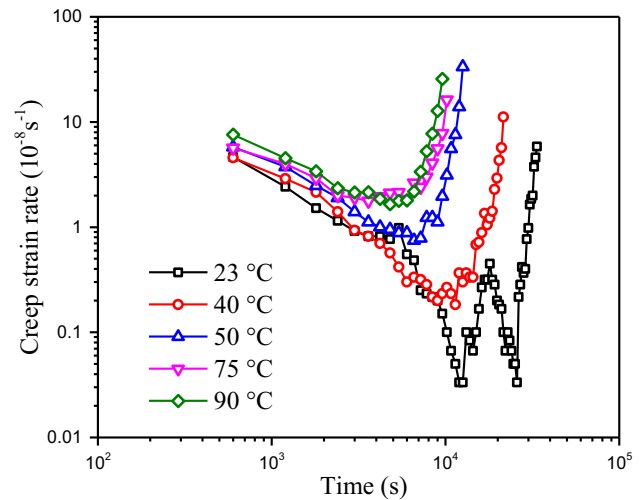

Fig. 11 The evolution of creep strain rate during deformation at a constant stress ($\sigma_y = 150$ MPa) for simulations performed under uniaxial conditions ($\sigma_x = 0$ MPa) at constant temperatures of 23, 40, 50, 75, and 90 °C

seen in laboratory experiments (Brantut et al. 2013). From these simulations, we can see that there is a clear temperature effect on brittle creep in granite.

We first note that the creep strain rate (the strain rate calculated during deformation at constant stress) strongly depends on temperature, as observed in brittle creep experiments (Heap et al. 2009a; Chen et al. 2015; Ye et al. 2015). The evolution of creep strain rate with time at various constant temperatures is shown in Fig. 11. The strain rate first decreases, reaches a minimum value (the minimum creep strain rate), and finally increases as the sample approaches macroscopic failure (Fig. 11). The simulations show that the minimum strain rate is much higher at higher temperatures. Indeed, there are several orders of magnitude difference in the minimum creep strain rate between the simulations performed at 23 and 90 °C (Fig. 11).

The large increase in strain rate at higher temperature also results in a large decrease in the time-to-failure (Fig. 12), as observed in experiments on granite (Kranz et al. 1982). For example, the sample at room temperature (23 °C) failed after about 35,000 s; time-to-failure was reduced to about 10,000 s at a temperature of 90 °C (Fig. 12). These simulations reveal that a small change in temperature results in large changes in creep strain rate and time-to-failure. We note that the reductions in time-to-failure observed experimentally for Barre granite by Kranz et al. (1982) are much larger than those reported here. Kranz et al. (1982) found that time-to-failure is reduced by a couple of orders of magnitude upon increasing the temperature from 24 to 200 °C. The smaller difference in time-to-failure seen in our simulations, compared to the
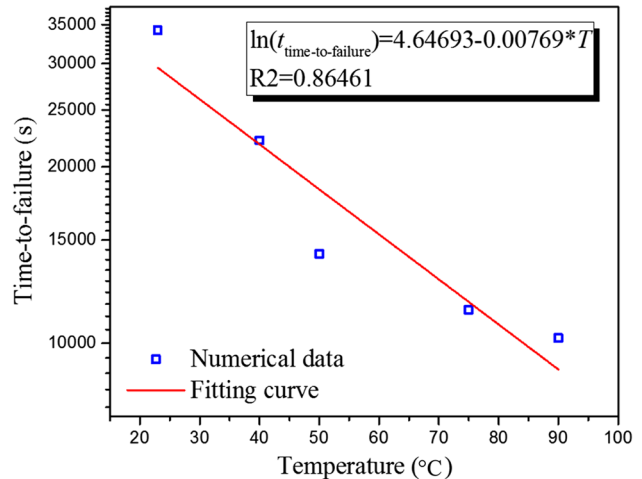

Fig. 12 Time-to-failure as a function of temperature for simulations performed under uniaxial conditions ($\sigma_x = 0$ MPa) at constant temperatures of 23, 40, 50, 75, and 90 °C. All simulations were performed under the same constant differential stress ($\sigma_y = 150$ MPa)

experiments of Kranz et al. (1982), is likely due to differences in the ratio of the creep stress and the short-term failure stress. The simulations provided here were performed at a constant differential stress that is 92.5% of the short-term failure stress. We anticipate that greater differences in time-to-failure as temperature is increased will be observed at lower stresses, as suggested by the experiments of Kranz et al. (1982).

5.3 Effect of Differential Stress

Here we show the results of a suite of conventional brittle creep experiments under different constant applied

differential stresses (i.e., we changed the ratio between the creep stress and the short-term failure stress) to study the effect of differential stress on brittle creep in granite. We performed uniaxial creep simulations at a constant temperature of 50 °C but various constant axial stresses of 140, 145, 150, 155, and 160 MPa. Figure 13 shows the numerically obtained creep curves for the five simulations. As before, the creep curves presented in Fig. 13 clearly show the accelerating–decelerating phenomenology of brittle creep seen in laboratory experiments (Brantut et al. 2013). These simulations highlight that the applied differential stress has a strong influence on brittle creep in granite, as seen in brittle creep experiments (e.g., Brantut et al. 2013). First, the creep strain rate is higher when the differential stress is higher (Fig. 14). Indeed, a change in differential stress from 140 to 160 MPa increases the minimum strain rate by over an order of magnitude (Fig. 14). Increases in strain rate of this magnitude for small (5–10 MPa) increases in the differential stress have been observed experimentally for many common rock types (Heap et al. 2009b; Brantut et al. 2013). As a result of the higher strain rate at higher differential stress, the time-to-failure is reduced as differential stress is increased (Fig. 15). For example, the time-to-failure at a differential stress of 140 MPa is more than 30,000 s, but is reduced to about 5000 s when the differential stress is increased to 160 MPa (Fig. 15).

Furthermore, we use the proposed model to perform brittle creep simulations under different constant confining pressures of 0, 2, and 10 MPa, but the same constant temperature and applied axial stress of 50 °C and 150 MPa, respectively. As for the previous simulations, the brittle creep curves (Fig. 16) capture the decelerating–
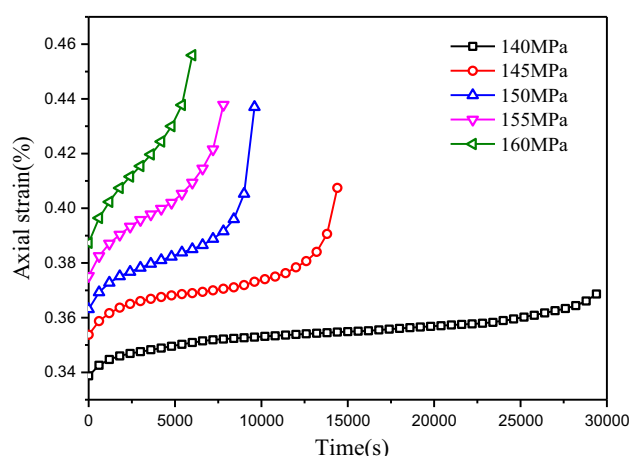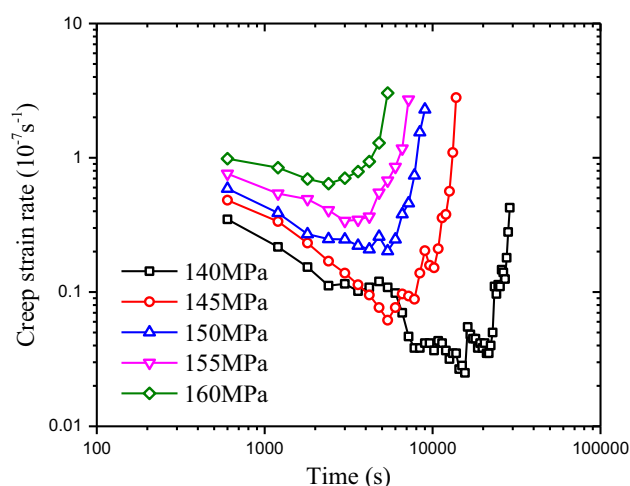

Fig. 14 The evolution of creep strain rate as a function of time for simulations performed under uniaxial conditions ($\sigma_x = 0$ MPa) at constant differential stresses (σ_y) between 140 and 160 MPa. All simulations were performed under the same constant temperature (50 °C)

accelerating phenomenology of laboratory brittle creep experiments (Brantut et al. 2013). These simulations highlight that confining pressure has a strong influence on brittle creep in granite. First, the creep strain rate is lower when the confining pressure is higher (Fig. 17): an increase in confining pressure from 0 to 10 MPa reduces the minimum strain rate by about an order of magnitude, results consistent with those from brittle creep experiments performed at different confining pressures (Heap et al. 2009b, Brantut et al. 2013). As a result of the lower strain rate at higher confining pressure, the time-to-failure is increased as confining pressure is increased. For example, the time-
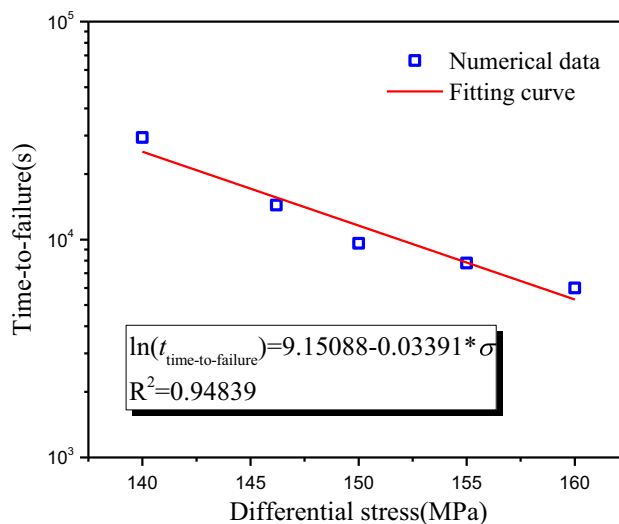

Fig. 13 Creep curves (axial strain as a function of time) for simulations performed under uniaxial conditions ($\sigma_x = 0$ MPa) at constant differential stresses (σ_y) between 140 and 160 MPa. All simulations were performed under the same constant temperature (50 °C)

Fig. 15 Time-to-failure as a function of temperature for simulations performed under uniaxial conditions ($\sigma_x = 0$ MPa) at constant differential stresses (σ_y) between 140 and 160 MPa. All simulations were performed under the same constant temperature (50 °C)

In the Fig. 15 inset:
$$\ln(t_{\text{time-to-failure}}) = 9.15088 - 0.03391 * \sigma$$
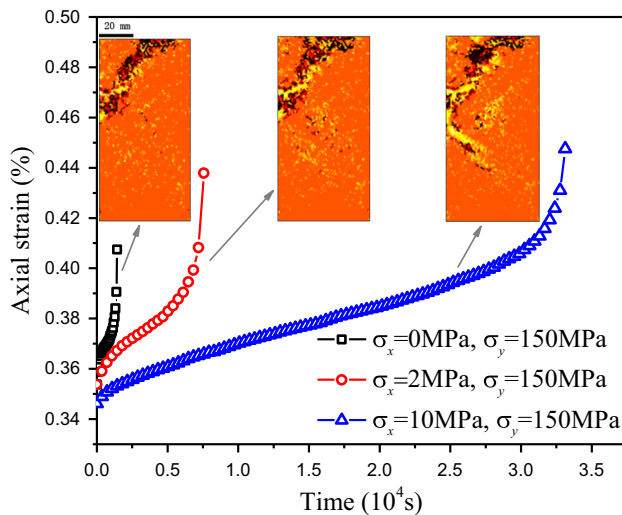$$R^2 = 0.94839$$

Fig. 16 Creep curves (axial strain as a function of time) for simulations performed under a constant differential stress (σ_y) of 150 MPa and confining pressures (σ_x) of 0, 2, and 10 MPa. All simulations were performed under the same constant temperature (50 °C)
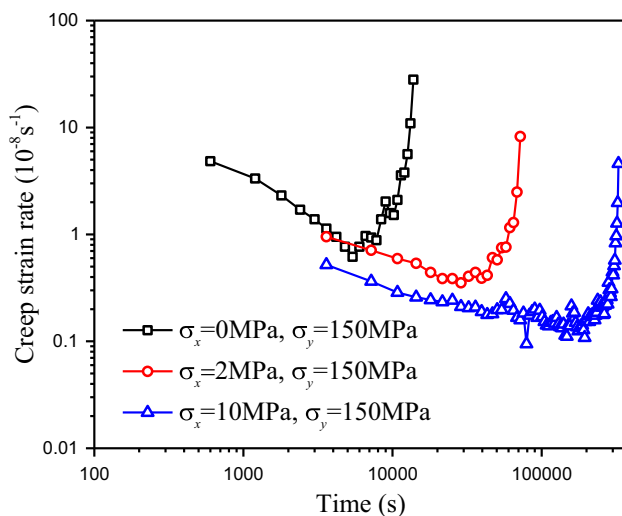

Fig. 17 Evolution of creep strain rate as a function of time for simulations performed under a constant differential stress (σ_y) of 150 MPa and confining pressures (σ_x) of 0, 2, and 10 MPa. All simulations were performed under the same constant temperature (50 °C)

to-failure under uniaxial conditions is about 30,000 s, but is increased to about 330,000 s when the confining pressure is increased to 10 MPa. Therefore, even modest increases in the confining pressure can significantly change the magnitude of the creep strain rate and time-to-failure, as observed experimentally (Heap et al. 2009b; Brantut et al. 2013).

Figure 16 also shows snapshots of each of the failed samples (black represents tensile damage, while yellow

represents shear damage). It can be seen that more localized shear damage occurred at higher confining pressures (Fig. 16).

5.4 Effect of Sample Heterogeneity

It is well known that rock is a heterogeneous material. It is for this reason we use a Weibull statistic distribution to reproduce mechanical heterogeneity within a realistic rock medium. To examine the effect of sample homogeneity on brittle creep in granite, a set of simulations were performed using different homogeneity indices of $\chi = 4$, 5, and 6 were performed (at a temperature of 50 °C, confining pressure of 0 MPa, and constant applied axial stress of 150 MPa). In these simulations, we keep the mean Young's modulus and mean UCS of the elements the same (43 GPa and 350 MPa, respectively; Table 1) and simply change the homogeneity index. As explained above, a larger homogeneity index implies that the elements within the sample will be closer to the mean value of 350 MPa (see Eq. (1) and Fig. 1). Therefore, a sample characterized by a larger homogeneity index will contain fewer low-strength elements and will be stronger and more brittle as a result. In reality, a decrease in the homogeneity index could reflect, for example, weathering of the feldspar within the granite (weathering typical of granites within geothermal reservoirs, e.g., Azaroual and Fouillac 1997).

The simulated creep curves (Fig. 18) and the evolution of creep strain rate as a function of time (Fig. 19) show that an increase in sample homogeneity leads to a decrease in creep strain rate and a corresponding increase in time-to-failure. For example, the minimum creep strain rate decreases by about an order of magnitude and the time-to-failure increases from about 111,600 to 358,200 s as the homogeneity index is increased from 4 to 6 (Figs. 18, 19). Decreasing sample homogeneity naturally has the opposite effect, resulting in increases and decreases to the creep strain rate and the time-to-failure, respectively.

6 Concluding Remarks

We have formulated a numerical model to simulate brittle creep in low-porosity granite under different loading conditions (differential stress and confining pressure) and different temperatures. In order to reflect the material heterogeneity at a mesoscale, the mechanical parameters (e.g., strength and Young's modulus) of the mesoscopic material elements, which are assumed to be homogeneous and isotropic, are assigned randomly using a Weibull statistic distribution. Importantly, the model introduces the concept of a mesoscopic renormalization to capture the co-operative interaction between microcracks in the transition
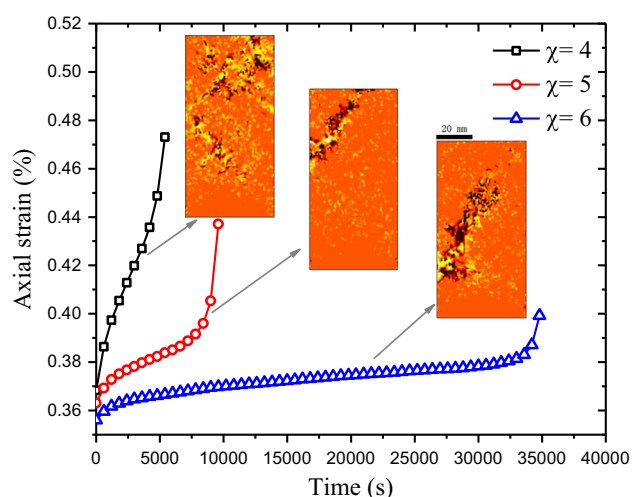
Fig. 18 Creep curves (axial strain as a function of time) for simulations performed on granite samples characterized by a different homogeneity index. All simulations were performed under the same differential stress ($\sigma_y = 150$ MPa), temperature (50 °C), and confining pressure ($\sigma_x = 0$ MPa)
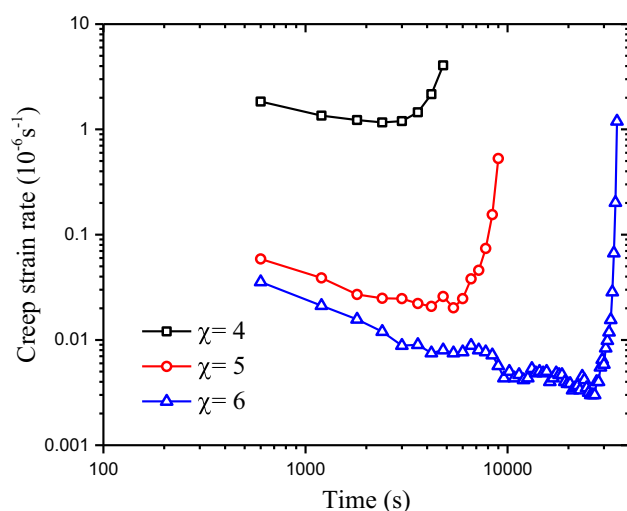

Fig. 19 The evolution of creep strain rate for simulations performed on granite samples characterized by a different homogeneity index. All simulations were performed under the same differential stress ($\sigma_y = 150$ MPa), temperature (50 °C), and confining pressure ($\sigma_x = 0$ MPa)

from distributed to localized damage. We validated our model using previously published experimental data and then used it to simulate conventional brittle creep experiments at various constant temperatures, applied differential stresses, confining pressures, and sample homogeneities. Our simulations accurately capture the short- and long-term mechanical behavior of the experimental data using unique thermo-physico-mechanical properties, lending confidence to our numerical approach. Our simulations show that: (1) increases in temperature and differential stress increase the creep strain rate and therefore reduce

time-to-failure and (2) increases in confining pressure and sample homogeneity decrease creep strain rate and increase time-to-failure. We anticipate that the modeling presented herein will assist in the management and optimization of geotechnical engineering projects within granite.

References

Aker E, Kühn D, Vavryčuk V, Soldal M, Oye V (2014) Experimental investigation of acoustic emissions and their moment tensors in rock during failure. Int J Rock Mech Min Sci 70:286–295

Amitrano D, Helmstetter A (2006) Brittle creep, damage, and time to failure in rocks. J Geophys Res B Solid Earth 111:1–17

Atkinson BK (1984) Subcritical crack growth in geological materials. J Geophys Res 89:4077–4114

Azaroual M, Fouillac C (1997) Experimental study and modelling of granite-distilled water interactions at 180 C and 14 bars. Appl Geochem 12(1):55–73

Baria R, Baumgärtner J, Gérard A, Jung R, Garnish J (1999) European HDR research programme at Soultz-sous-Forêts (France) 1987–1996. Geothermics 28:655–669

Baud P, Meredith PG (1997) Damage accumulation during triaxial creep of darley dale sandstone from pore volumometry and acoustic emission. Int J Rock Mech Min Sci 34:24.e1–24.e10

Benson PM, Meredith PG, Schubnel A (2006) Role of void space geometry in permeability evolution in crustal rocks at elevated pressure. J Geophys Res Solid Earth 111(B12):1–14

Berard T, Cornet FH (2003) Evidence of thermally induced borehole elongation: a case study at Soultz, France. Int J Rock Mech Min Sci 40(7):1121–1140

Bikong C, Hoxha D, Shao JF (2015) A micro-macro model for time-dependent behavior of clayey rocks due to anisotropic propagation of microcracks. Int J Plast 69:73–88

Brantut N, Heap MJ, Meredith PG, Baud P (2013) Time-dependent cracking and brittle creep in crustal rocks: a review. J Struct Geol 52:17–43

Brantut N, Heap MJ, Baud P, Meredith PG (2014) Mechanisms of time-dependent deformation in porous limestone. J Geophys Res Solid Earth 119:5444–5463

Carter NL, Hansen FD (1983) Creep of rocksalt. Tectonophysics 92:275–333

Chen L, Liu JF, Wang CP, Wang L, Wang XY, Wang J (2012) Study of acoustic emission characteristics of Beishan deep granite under different stress conditions. Chin J Rock Mech Eng 31:3618–3624

Chen Y, Hu S, Wei K, Hu R, Zhou C, Jing L (2014) Experimental characterization and micromechanical modeling of damage-induced permeability variation in Beishan granite. Int J Rock Mech Min Sci 71:64–76

Chen L, Liu JF, Wang CP, Liu J, Wang J (2015) Experimental investigation on the creep behaviour of Beishan granite under different temperature and stress conditions. Eur J Environ Civ Eng 19:s43–s53

Chen L, Wang CP, Liu JF, Li Y, Liu J, Wang J (2017) Effects of temperature and stress on the time-dependent behavior of Beishan granite. Int J Rock Mech Min Sci 93:316–323

Chu S, Majumdar A (2012) Opportunities and challenges for a sustainable energy future. Nature 488:294–303

Clauser C, Huenges E (1995) Thermal conductivity of rocks and minerals. In: Ahrens TJ (ed) Rock physics & phase relations: a handbook of physical constants. American Geophysical Union, Washington, DC, pp 105–126

Cristescu N (1993) A general constitutive equation for transient and stationary creep of rock salt. Int J Rock Mech Min Sci Geomech Abstr 30:125–140

Dubey RK, Gairola VK (2008) Influence of structural anisotropy on creep of rocksalt from Simla Himalaya, India: an experimental approach. J Struct Geol 30:710–718

Fortin J, Stanchits S, Dresen G, Gueguen Y (2009) Acoustic emissions monitoring during inelastic deformation of porous sandstone: comparison of three modes of deformation. Pure Appl Geophys 166:823–841

Fujii Y, Kiyama T, Ishijima Y, Kodama J (1999) Circumferential strain behavior during creep tests of brittle rocks. Int J Rock Mech Min Sci 36:323–337

Gibb FGF (2000) A new scheme for the very deep geological disposal of high-level radioactive waste. J Geol Soc 157:27–36

Golshani A, Okui Y, Oda M, Takemura T (2006) A micromechanical model for brittle failure of rock and its relation to crack growth observed in triaxial compression tests of granite. Mech Mater 38:287–303

Griffiths L, Heap MJ, Xu T, Chen CF, Baud P (2017) The influence of pore geometry and orientation on the strength and stiffness of porous rock. J Struct Geol 96:149–160

Heap MJ, Baud P, Meredith PG (2009a) Influence of temperature on brittle creep in sandstones. Geophys Res Lett 36:L19305

Heap MJ, Baud P, Meredith PG, Bell AF, Main IG (2009b) Time-dependent brittle creep in Darley Dale sandstone. J Geophys Res 114:1–22

Heap MJ, Baud P, Meredith PG, Vinciguerra S, Bell AF, Main IG (2011) Brittle creep in basalt and its application to time-dependent volcano deformation. Earth Planet Sci Lett 307:71–82

Heap MJ, Brantut N, Baud P, Meredith PG (2015) Time-dependent compaction band formation in sandstone. Br J Forensic Pract 11:3–7

Heap MJ, Wadsworth FB, Xu T, Chen CF (2016) The strength of heterogeneous volcanic rocks: a 2D approximation. J Volcanol Geotherm Res 319:1–11

Heard HC (1976) Comparison of the flow properties of rocks at crustal conditions. Philos Trans R Soc Lond Ser A Math Phys Sci 283:173–186

Heuze FE (1983) High-temperature mechanical, physical and thermal properties of granitic rocks—a review. Int J Rock Mech Min Sci Geomech Abstr 20:3–10

Homand-Etienne F, Hoxha D, Shao JF (1998) A continuum damage constitutive law for brittle rocks. Comput Geotech 22:135–151

Jeager JC, Cook NGW, Zimmerman R (eds) (2007) Fundamentals of rock mechanics. Wiley-Blackwell, Singapore

Katz O, Reches Z (2002) Pre-failure damage, time-dependent creep and strength variations of a brittle granite. In: Proceedings of the fifth International conference on anal discontinuous deformation, Ben-Gurion University, Balkema, Rotterdam

Khelifa M, Oudjene M, Khennane A (2007) Fracture in sheet metal forming: effect of ductile damage evolution. Comput Struct 85:205–212

Krajcinovic D (2000) Damage mechanics: accomplishments, trends and needs. Int J Solids Struct 37:267–277

Kranz RL (1980) The effects of confining pressure and stress difference on static fatigue of granite. J Geophys Res 85:1854–1866

Kranz RL, Scholz CH (1977) Critical dilatant volume of rocks at the onset of tertiary creep. J Geophys Res 82:4893–4898

Kranz RL, Harris WJ, Carter NL (1982) Static fatigue of granite at 200°C. Geophys Res Lett 9:1–4

Kraus H (1980) Creep analysis. Wiley, New York

Lajtai EZ, Schmidtke RH (1986) Delayed failure in rock loaded in uniaxial compression. Rock Mech Rock Eng 19:11–25

Lemaitre J, Desmorat R (2005) Engineering damage mechanics. Springer, Berlin

Lin QX, Liu YM, Tham LG, Tang CA, Lee PKK, Wang J (2009) Time-dependent strength degradation of granite. Int J Rock Mech Min Sci 46:1103–1114

Lockner D (1993a) The role of acoustic-emission in the study of rock fracture. Int J Rock Mech Min Sci 30:883–899

Lockner D (1993b) Room temperature creep in saturated granite. J Geophys Res 98:475–487

Lockner DA, Madden TR (1991) A multiple-crack model of brittle-fracture. 2. Time-dependent simulations. J Geophys Res B Solid Earth 96:19643–19654

Lu C, Danzer R, Fischer FD (2002) Fracture statistics of brittle materials: Weibull or normal distribution. Phys Rev E 65:067102

Lu Y, Elsworth D, Wang L (2014) A dual-scale approach to model time-dependent deformation, creep and fracturing of brittle rocks. Comput Geotech 60:61–76

Maranini E, Yamaguchi T (2001) A non-associated viscoplastic model for the behaviour of granite in triaxial compression. Mech Mater 33:283–293

Meredith PG, Atkinson BK (1983) Stress corrosion and acoustic emission during tensile crack propagation in Whin Sill dolerite and other basic rocks. Geophys J Int 75:1–21

Nara Y, Hiroyoshi N, Yoneda T, Kaneko K (2010) Effects of relative humidity and temperature on subcritical crack growth in igneous rock. Int J Rock Mech Min Sci 47:640–646

Nara Y, Kato H, Yoneda T, Kaneko K (2011a) Determination of three-dimensional microcrack distribution and principal axes for granite using a polyhedral specimen. Int J Rock Mech Min Sci 48:316–335

Nara Y, Morimoto K, Yoneda T, Hiroyoshi N, Kaneko K (2011b) Effects of humidity and temperature on subcritical crack growth in sandstone. Int J Solids Struct 48:1130–1140

Ohnaka M (1983) Acoustic emission during creep of brittle rock. Int J Rock Mech Min Sci Geomech Abstr 20:121–134

Qi M, Shao JF, Giraud A, Zhu QZ, Colliat JB (2016) Damage and plastic friction in initially anisotropic quasi brittle materials. Int J Plast 82:260–282

Sano O, Kudo Y, Mizuta Y (1992) Experimental determination of elastic constants of Oshima granite, Barre granite, and Chelmsford granite. J Geophys Res Solid Earth 97:3367–3379

Schubnel A, Walker E, Thompson BD, Fortin J, Guéguen Y, Young RP (2006) Transient creep, aseismic damage and slow failure in Carrara marble deformed across the brittle-ductile transition. Geophys Res Lett 33:L17301

Shao JF, Duveau G, Hoteit N, Sibai M, Bart M (1997) Time dependent continuous damage model for deformation and failure of brittle rock. Int J Rock Mech Min Sci 34:285.e1–285.e213

Shao JF, Zhu QZ, Su K (2003) Modeling of creep in rock materials in terms of material degradation. Comput Geotech 30:549–555

Shao JF, Chau KT, Feng XT (2006) Modeling of anisotropic damage and creep deformation in brittle rocks. Int J Rock Mech Min Sci 43:582–592

Sornette D, Vanneste C, Knopoff L (1992) Statistical model of earthquake foreshocks. Phys Rev A 45:8351

Surma F, Geraud Y (2003) Porosity and thermal conductivity of the Soultz-sous-Forêts granite. Pure Appl Geophys 160:1125–1136

Tang CA (1997) Numerical simulation of progressive rock failure and associated seismicity. Int J Rock Mech Min Sci 34:249–261

Townend E, Thompson BD, Benson PM, Meredith PG, Baud P, Young RP (2008) Imaging compaction band propagation in Diemelstadt sandstone using acoustic emission locations. Geophys Res Lett 35:1–5

Vázquez-Prada M, Gómez J, Moreno Y, Pacheco A (1999) Time to failure of hierarchical load-transfer models of fracture. Phys Rev E 60:2581

Voight B (1989) A relation to describe rate-dependent material failure. Science 243:200–203

Wang J, Su R, Chen W, Guo Y, Jin Y, Wen Z, Liu Y (2006) Deep geological disposal of high-level radioactive wastes in China. Chin J Rock Mech Eng 25(4):649–658

Wang C, Chen L, Liu J, Liu J (2015) Experimental characterisation of thermo-mechanical coupling properties of Beishan granite. Eur J Environ Civ Eng 19:s29–s42

Wedepohl KH (1995) The composition of the continental crust. Geochim Cosmochim Acta 59(7):1217–1232

Weibull W (1951) A statistical distribution function of wide applicability. J Appl Mech 18:293–297

Weiss J, Marsan D (2003) Three-dimensional mapping of dislocation avalanches: clustering and space/time coupling. Science 299:89–92

Wong T-F, David C, Zhu W (1997) The transition from brittle faulting to cataclastic flow in porous sandstones: mechanical deformation. J Geophys Res 102:3009–3025

Wong T-F, Wong RHC, Chau KT, Tang CA (2006) Microcrack statistics, Weibull distribution and micromechanical modeling of compressive failure in rock. Mech Mater 38:664–681

Xu T, Tang CA, Zhao J, Li LC, Heap MJ (2012) Modelling the time-dependent rheological behaviour of heterogeneous brittle rocks. Geophys J Int 189:1781–1796

Xu T, Ranjith P, Wasantha P, Zhao J, Tang C, Zhu W (2013) Influence of the geometry of partially-spanning joints on mechanical properties of rock in uniaxial compression. Eng Geol 167:134–147

Yang Q, Cox B (2005) Cohesive models for damage evolution in laminated composites. Int J Fract 133:107–137

Yang S-Q, Jing H-W, Cheng L (2014) Influences of pore pressure on short-term and creep mechanical behavior of red sandstone. Eng Geol 179:10–23

Ye GL, Nishimura T, Zhang F (2015) Experimental study on shear and creep behaviour of green tuff at high temperatures. Int J Rock Mech Min Sci 79:19–28

Yoshida H, Horii H (1992) A micromechanics-based model for creep behavior of rock. Appl Mech Rev 45:294–303

Zhao XG, Cai M, Wang J, Ma LK (2013) Damage stress and acoustic emission characteristics of the Beishan granite. Int J Rock Mech Min Sci 64:258–269

Zhao LY, Zhu QZ, Xu WY, Dai F, Shao JF (2016) A unified micromechanics-based damage model for instantaneous and time-dependent behaviors of brittle rocks. Int J Rock Mech Min Sci 84:187–196

Zhu QZ, Shao JF (2015) A refined micromechanical damage–friction model with strength prediction for rock-like materials under compression. Int J Solids Struct 60–61:75–83

Zhu WC, Wei J, Zhao J, Niu LL (2014) 2D numerical simulation on excavation damaged zone induced by dynamic stress redistribution. Tunn Undergr Space Technol 43:315–326

Zitnay JL, Li Y, Qin Z, San BH, Depalle B, Reese SP, Buehler MJ, Yu SM, Weiss JA (2017) Molecular level detection and localization of mechanical damage in collagen enabled by collagen hybridizing peptides. Nat Commun 8:14913

Zong ZH, Ma LK, Gao M, Tian X (2013) Study on acoustic emission characteristics of Beishan granite under triaxial compression conditions. Uranium Geol 29:123–128